Geophysical Journal International

Geophys. J. Int. (2018) **214,** 2250–2263
Advance Access publication 2018 June 19
GJI Geodynamics and tectonics

doi: 10.1093/gji/ggy240

Uncertainty reduction of stress tensor inversion with data-driven catalogue selection

S. von Specht,[1,2] O. Heidbach,[2] F. Cotton[1,2] and A. Zang[1,2]

[1] *Institute of Earth and Environmental Science, University of Potsdam, Potsdam 14476, Germany. E-mail: sspecht@uni-potsdam.de*
[2] *Helmholtz Centre Potsdam GFZ German Research Centre for Geosciences, Potsdam 14473, Germany*

Accepted 2018 June 18. Received 2017 November 8; in original form 2018 June 14

SUMMARY

The selection of earthquake focal mechanisms (FMs) for stress tensor inversion (STI) is commonly done on a spatial basis, that is, hypocentres. However, this selection approach may include data that are undesired, for example, by mixing events that are caused by different stress tensors when for the STI a single stress tensor is assumed. Due to the significant increase of FM data in the past decades, objective data-driven data selection is feasible, allowing more refined FM catalogues that avoid these issues and provide data weights for the STI routines. We present the application of angular classification with expectation-maximization (ACE) as a tool for data selection. ACE identifies clusters of FM without *a priori* information. The identified clusters can be used for the classification of the style-of-faulting and as weights of the FM data. We demonstrate that ACE effectively selects data that can be associated with a single stress tensor. Two application examples are given for weighted STI from South America. We use the resulting clusters and weights as *a priori* information for an STI for these regions and show that uncertainties of the stress tensor estimates are reduced significantly.

Key words: Inverse Theory; Statistical Methods; Seismicity; tectonics; Kinematics of crustal; mantle deformation.

1 INTRODUCTION

Understanding Earth's stress field provides insight into rupture mechanics of earthquakes and tectonic deformation processes in general. Stress itself cannot be observed directly and thus must be inferred from kinematic deformation. Earthquake focal mechanisms (FMs) are of key importance to derive deformation within the Earth and thus allow inference of stress orientations.

Stress tensor inversion (STI) methods have been published since the 1970s (Carey-Gailhardis & Brunier 1974; Angelier 1979; Armijo *et al.* 1982; Rivera & Cisternas 1990). Due to their significance for stress tensor inference, several methods have been proposed to invert for the stress tensor from FM data alone. The three major routines used today are based on the works of Angelier (1979), Michael (1984) and Gephart & Forsyth (1984). Maury *et al.* (2013) provide a comprehensive overview and comparison of these methods and summarize their common assumptions:

(1) Slip orientation is parallel to the resolved shear stress orientation on the rupture plane. This assumption is known as the Wallace–Bott hypothesis (Wallace 1951; Bott 1959).

(2) The medium in which the FM occurred is homogeneous, that is, the stress is assumed to be constant in the entire volume and all ruptures are related to a single stress tensor.

(3) Earthquakes are independent from each other. This assumption is linked to the previous assumption insofar, as a major earthquake temporarily alters the regional stress tensor. Aftershocks are therefore not only influenced by the background stress field, but also by the variation to it from the main shock.

The methods based on Angelier (1979) and Michael (1984) are based on the L_2-norm, that is, least squares (LSQ). The large data variability in FMs leads Gephart & Forsyth (1984) to use an L_1-norm, that is, least absolute deviation (LAD), to reduce the impact of outliers. Several advancements have been proposed on the basis of these three methods, including spatial variations (Hardebeck & Michael 2006; Maury *et al.* 2013; Martínez-Garzón *et al.* 2016), identification of slip directions (e.g. Lund & Slunga 1999; Xu 2004; Vavryčuk 2011), inversion independent of nodal plane identification (Angelier 2002) and uncertainty estimation (Hardebeck & Hauksson 2001a).

Though advances have been made in the inversion routines, the basic aspect of data selection has not been addressed to a larger extent. The most common approach is to select data from spatial regions. The regional binning can be based on different criteria. Townend & Zoback (2001) used rectangular zones of different sizes, while Hardebeck & Michael (2004) defined stripes parallel to major fault zones (e.g. the San Andreas fault Hardebeck & Hauksson

1999). Hardebeck & Hauksson (2001b) also used temporal binning. This kind of data binning is insofar a deterministic choice as it implies the same stress tensor for all FMs in a given bin. Data not following this assumption appear as outliers and enlarge the uncertainties of the inversion results. Hardebeck & Michael (2004) demonstrated large variations in stress tensor orientations due to different binning strategies. In addition to assumption of the constant stress tensor in a given bin, the FM data related to that stress tensor should be diverse to properly represent displacement associated with the given stress tensor (Hardebeck & Michael 2004). This poses a trade-off in any STI: To only include FM data that are related to a single stress tensor, the bin should be as small as possible. However, the same bin must be large enough to contain a variety of different FM to reduce the bias of the inversion.

Different approaches to the relaxation of the constant stress tensor assumption have been proposed, as spatial variations of the stress field have been documented even on local scale (Hardebeck & Hauksson 1999). Michael (1991) superposes several stress tensors in a region; an approach similar to Armijo *et al.* (1982), where the data are grouped into different tectonic phases to minimize the stress ratio. Spatial subdivision has been proposed by Hardebeck & Michael (2006) by horizontally subdividing the region of interest into linearly dependent spatial bins. Maury *et al.* (2013) incorporated a linear variability of stress with depth.

In recent years, more advanced data selection criteria have been published. García *et al.* (2012) introduced a selection framework for the development of ground motion prediction equations that can also be applied to data selection for stress modelling. The data-driven binning technique by Martínez-Garzón *et al.* (2016) is based on Voronoi tessellation, which subdivides the region of interest into irregularly shaped convex subregions. In either case data selection is deterministic, as a datum is included in the set or not.

In this paper, we present a non-deterministic data selection approach introducing data weighting. The general concept of data weighting in STI has already been proposed by Armijo *et al.* (1982) by incorporating the uncertainties of the data and the model. Due to the unknown model uncertainties, the data and model uncertainties are represented by a single ratio. This ratio is treated as a free parameter resulting in a damped LSQ solution.

The data weights we use are based on angular classification with expectation-maximization (ACE), a probabilistic FM cluster analysis (Specht *et al.* 2017). ACE determines the FM cluster parameters and the number of FM clusters. The algorithm identifies FM clusters for both nodal planes. Clusters can be associated with different stress tensors (e.g. at a plate interface). Data which cannot be associated with any cluster are unclassified. The probabilities of each nodal plane pair (i.e. FM) to belong to a particular stress tensor can be directly used as weights. Event classification is not directly dependent on the event's hypocentre because ACE is based on the FM angles alone. Therefore, ACE also provides a binning strategy for data selection independent of the spatial distribution—the most common approach of data selection in STI.

The down-weighted data from ACE are demonstrated to be outliers which have a higher influence on the inversion outcome. If data originate from a region with several stress tensors, ambiguities arise when assigning FM to a specific stress tensor. This ambiguity is important and needs to be considered when selecting data to accommodate the data diversity and reduce inversion bias.

The application of data-driven data selection has become feasible with the steady increase of FM catalogues over the last decades. During the pioneering times of STI—when data were scarce and data picking was out of the question—every available datum was used in the inversion. However, with catalogues covering tens of thousands of FM the data selection in general can be improved as well as STI.

We briefly review the STI routine of Michael (1984) and its spatial extension (Hardebeck & Michael 2006) and how data weighting is incorporated into both models (Section 2). The applicability of data weighting and its impact on synthetic FM catalogues is shown in Section 3. In Section 4, we present two applications of the weighted STI by applying to data from South America.

2 METHODS

In this section, we first briefly review the theoretical framework of inverse theory which is the basis for all STI routines. We focus on data leverage in a model and its impact on inversion results and on how to mitigate the effects of highly self-sensitive data with data weighting. In Section 2.2, we review the STI routines of Michael (1984) and Hardebeck & Michael (2006) and how they can be augmented with data weighting.

2.1 Basics

The common approach to inferring the stress field is to align the stress tensor, such that, the differences of the observed displacement (e.g. in the form of FMs) to the modelled displacement are overall minimized. This formulation can be expressed in its simplest form by the objective function:

$$S = \sum_{i=1}^{n} |d_i - s_i|^p, \tag{1}$$

where s and d are the observed and modelled data, respectively. The exponent p defines the weighting norm. The inversion routines by Angelier (1979) and Michael (1984) use $p = 2$ (LSQ), while Gephart & Forsyth (1984) use $p = 1$ (LAD). The data type in the objective function differs for all routines, and is for generality not further specified here. The larger the p, the larger the impact of a large residual (i.e. outlier) on the objective function S and thus the outcome of the final model.

If $p = 2$ in eq. (1) then the objective function can also be represented in matrix notation as

$$S = (\mathbf{s} - \mathbf{d})^{\mathbf{T}}(\mathbf{s} - \mathbf{d}), \tag{2}$$

$$= (\mathbf{s} - \mathbf{At})^{\mathbf{T}}(\mathbf{s} - \mathbf{At}). \tag{3}$$

The matrix $\mathbf{A}$ is the design matrix containing the independent variables of the model and the functional form relating the model parameters $\mathbf{t}$ to the data $\mathbf{s}$. Data in $\mathbf{s}$ are therefore dependent variables. While the independent variables are assumed to be free of errors, the dependent variables are considered erroneous, that is, uncertain.

The objective function in eq. (3) can be generalized by Armijo *et al.* (1982), Tarantola (2005) and Menke (2012)

$$S = (\mathbf{s} - \mathbf{At})^{\mathbf{T}}\Omega^{-1}(\mathbf{s} - \mathbf{At}), \tag{4}$$

where the matrix Ω is the data covariance matrix representing data uncertainties. The general LSQ solution for $\mathbf{t}$ is given by :

$$\mathbf{t} = (\mathbf{A}^{\mathbf{T}}\Omega^{-1}\mathbf{A})^{-1}\mathbf{A}^{\mathbf{T}}\Omega^{-1}\mathbf{d}. \tag{5}$$

This relation expresses the model parameters in terms of the data. In the cases of the stress inversion routines by Angelier (1979) and Michael (1984), it holds that $\Omega^{-1} = \mathbf{I}$ (the identity matrix). This is the ordinary LSQ solution (eq. 3) and implies that all data

are equally reliable (erroneous). The method by Angelier (1979) includes a second constraint in eq. (4) (see Xu 2004, for expressing this in matrix notation), as does the inversion routine of Armijo *et al.* (1982). The L_1-norm used by Gephart & Forsyth (1984) can be expressed by reweighting the data in Ω^{-1} (Hill & Holland 1977; Holland & Welsch 1977; Street *et al.* 1988); the data themselves are treated as in the cases for Angelier (1979) and Michael (1984), that is, equally reliable. In most cases the true uncertainties of the data are neither known nor included.

Because the model parameters are derived from all data, it is reasonable to investigate how the observed data **d** influence the outcome of the modelled data **s** (Cook 1977; Hoaglin & Welsch 1978; Cardinali *et al.* 2004; Menke 2012). A relation between **d** and **s** results by using eq. (5):

$$\mathbf{s} = \mathbf{A}\mathbf{t}, \tag{6}$$

$$= \mathbf{A}(\mathbf{A}^{\mathrm{T}}\Omega^{-1}\mathbf{A})^{-1}\mathbf{A}^{\mathrm{T}}\Omega^{-1}\mathbf{d}, \tag{7}$$

$$= \mathbf{N}\mathbf{d}. \tag{8}$$

The matrix **N** is known under different names [hat matrix (Hoaglin & Welsch 1978), data resolution matrix (Menke 2012), influence matrix (Cardinali *et al.* 2004)]. The elements of the data resolution matrix provides factors to express modelled data as a linear combination of observed data

$$s_i = \sum_{j=1}^{n} N_{ij} d_j. \tag{9}$$

The elements of the main diagonal of **N** are called importance (Menke 2012), self-influence/self-sensitivity (Cardinali *et al.* 2004), or leverage (Hoaglin & Welsch 1978). The leverage expresses how much each observed datum contributes to its own prediction.

We define a relative leverage based on eq. (9) as the ratio between the *i*th leverage and the sum of values of the *i*th row in the data resolution matrix:

$$N_i^{\mathrm{rel}} = \frac{n N_{ii}}{\sum_{j=1}^{n} N_{ij}}. \tag{10}$$

The relative leverage represents by how much more a datum influences its own prediction compared to the average absolute contribution of the data. If $N_i^{\mathrm{rel}} = 1$ then the datum's contribution is on average, if $N_i^{\mathrm{rel}} > 1$ the contribution is larger and if $N_i^{\mathrm{rel}} < 1$ the contribution is less than the average.

The leverage of the observed data **d** is not necessarily uniform for a given model **A**, that is, the model itself imposes different weighting on the data in the independent variables. Consider a simple line fit with LSQ:

$$y = ax + b. \tag{11}$$

Fig. 1 shows two line data sets (15 observations) and their respective LSQ solutions. Both data sets include one datum with identical error, but at different locations. The first data set has the error in the first (leftmost) datum (Fig. 1a; circles), the second in the eighth (central) datum (Fig. 1b; circles). Despite their high similarities both data sets yield different inversion results (Figs 1a and b; solid lines) not only in the parameters but also in the deviation from the true model. The reason for this difference is seen in the leverage of the data with respect to the model (Fig. 1c). In case of the simple line fit, leverage is lowest at the mean of the independent variables, ($\bar{x}$), and increases with distance to it. In this example, the outermost data

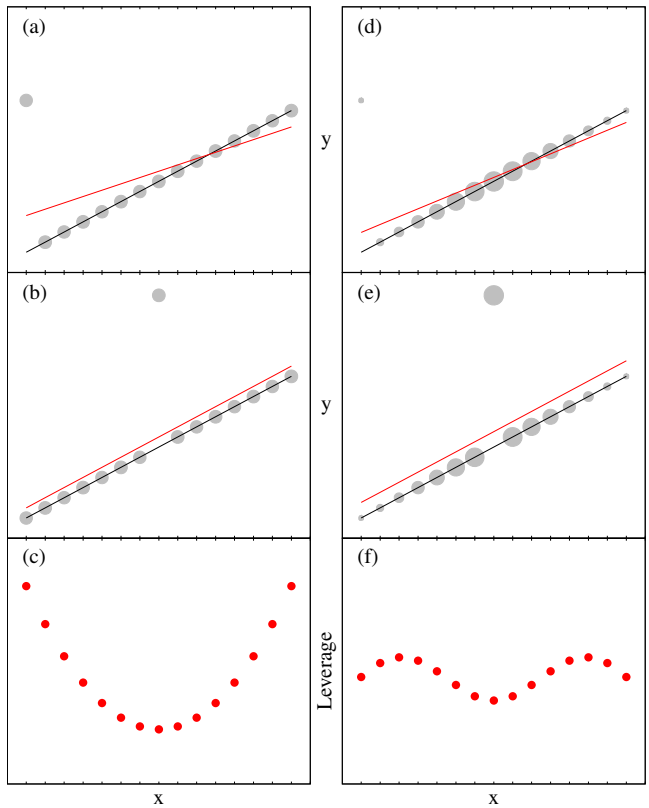

Figure 1. Comparison of ordinary LSQ (left-hand column) to weighted LSQ (WSLQ; right-hand column). In both cases the data originate from a straight line (black). In total 15 data points are sampled from this straight line (grey dots). In panels (a) and (d) an 'error' is introduced in the first datum by shifting. In panels (b) and (e) the error is introduced in the eighth datum. The error is the same in all cases. The ordinary LSQ solution (red) in panels (a) and (b) differs not only from the truth (black) due to the introduced error but also both solutions differ from each other. This solution difference depends on the leverage of the data (c). In case of ordinary LSQ for the straight line problem leverage follows a parabola, thus the data at both ends influence the model more than data in the middle. WLSQ can be used to redistribute leverage. In panels (d) and (e) the weights are represented by dot size and are the same in both cases. The straight line models in parts (d) and (e) differ less from each other than in the respective unweighted cases (a) and (b). While the model (red) in panel (d) is closer to the truth (black) than in panel (a), the model in panel (e) deviates more from the truth than in panel (b). Though the leverage of the WLSQ is more balanced (f) than for unweighted ordinary LSQ (c), that is, each datum has a similar impact on the model in panels (d) and (e), the decreased leverage at the ends of the data (d) results in an increased leverage in the data in the middle (e). WLSQ redistributes leverage and can therefore also be used to balance leverage.

points have more than three times higher influence on the model parameters than the data at the centre.

One way to mitigate the effects of outlying data and/or the high-leverage data is to introduce data weighting by using Ω^{-1} as a weight matrix, denoted by **W**:

$$S = (\mathbf{d} - \mathbf{s})^{\mathrm{T}}\mathbf{W}(\mathbf{d} - \mathbf{s}) \tag{12}$$

and

$$\mathbf{W} = \begin{pmatrix} w_1 & 0 & \cdots & 0 \\ 0 & w_2 & \cdots & 0 \\ \vdots & \vdots & \ddots & \vdots \\ 0 & 0 & \cdots & w_n \end{pmatrix}. \tag{13}$$

This definition is the weighted LSQ (WLSQ) solution (Menke 2012). A reduction of the impact of outliers in the dependent variable is achieved by LAD that can be realized with iteratively reweighted LSQ (Hill & Holland 1977; Holland & Welsch 1977; Street *et al.* 1988). Effects of leverage can be mitigated by taking the data distribution into account. For the straight line example from above one could define a weight function based on the difference $x_i - \bar{x}$, that is, the distance of an independent variable to the mean of the independent variable, for example,

$$w_i = \mathrm{e}^{-\left(\frac{x_i-\bar{x}}{b}\right)^2}, \tag{14}$$

where b is some user-based scaling factor. This function weights data close to $\bar{x}$ highest and less with increasing distance to $\bar{x}$.

The effect of such a weighting function on the straight line data is shown in the right-hand column of Fig. 1. The inversion for the data with the outlier in the outermost datum (Fig. 1d) deviates less from the original model than in the unweighted case (Fig. 1a). For data with the outlier in the central datum the deviation is slightly increased (Fig. 1a). However, both results of the weighted inversions are more similar to each other than in the unweighted case, that is, the leverage is more equally distributed due to the weighting. A weighting function redistributes leverage and can therefore be applied to balance the influence of data on the model parameters.

2.2 Stress tensor inversion

One of the most commonly used STI routines has been introduced by Michael (1984) which is a direct implementation of eq. (5)

$$\mathbf{s} = \mathbf{A}\mathbf{t}, \tag{15}$$

where $\mathbf{s}$ represents the unit slip vectors, matrix $\mathbf{A}$ is based on the normal vectors $\mathbf{n}$ and $\mathbf{t}$ is the deviatoric stress tensor in vector notation. This formulation implies that the slip magnitude is uniform in all directions as slip is represented by unit vectors and the relation to the 3×3 stress tensor $\boldsymbol{\sigma}$ is given by:

$$\mathbf{s} = \boldsymbol{\sigma}\mathbf{n} - (\boldsymbol{\sigma}\mathbf{n}\cdot\mathbf{n})\mathbf{n}. \tag{16}$$

The difference of the deviatoric stress tensor to the stress tensor $\boldsymbol{\sigma}$ is the absence of an isotropic stress component (pressure, p). The deviatoric stress tensor $\boldsymbol{\sigma}^{\mathrm{dev}}$ is defined by

$$\boldsymbol{\sigma}^{\mathrm{dev}} = \boldsymbol{\sigma} - p\mathbf{I}, \tag{17}$$

where $\mathbf{I}$ is the identity matrix and pressure p is

$$p = \frac{\mathrm{tr}(\boldsymbol{\sigma})}{3} = \frac{\sigma_{11}+\sigma_{22}+\sigma_{33}}{3}, \tag{18}$$

thus follows $\sigma_{33}^{\mathrm{dev}} = \sigma_{11}^{\mathrm{dev}} + \sigma_{22}^{\mathrm{dev}}$, that is, the deviatoric stress tensor has five independent components only. For convenience the stress tensor is expressed in Voigt notation

$$\mathbf{t} = \begin{pmatrix} t_1 \\ t_2 \\ t_3 \\ t_4 \\ t_5 \end{pmatrix} = \begin{pmatrix} \sigma_{11}^{\mathrm{dev}} \\ \sigma_{12}^{\mathrm{dev}} \\ \sigma_{13}^{\mathrm{dev}} \\ \sigma_{22}^{\mathrm{dev}} \\ \sigma_{23}^{\mathrm{dev}} \end{pmatrix} = \begin{pmatrix} \sigma_{11} - p \\ \sigma_{12} - p \\ \sigma_{13} \\ \sigma_{22} \\ \sigma_{23} \end{pmatrix}. \tag{19}$$

The eigenvectors of $\mathbf{t}$ represent the three principal stress orientations: S_1 for maximum, S_2 for intermediate and S_3 for minimum principal stress.

The matrix $\mathbf{A}_i$ is based on the normal vector $\mathbf{n}_i$ (subscript i dropped in the following equation) and follows from eq. (16)

$$\mathbf{A} = \begin{pmatrix} n_1 - n_1^3 + n_1 n_3^2 & -n_2 n_1^2 + n_2 n_3^2 & -n_3 n_1^2 - n_3 + n_3^3 \\ n_2 - 2n_2 n_1^2 & n_1 - 2n_1 n_2^2 & -2n_1 n_2 n_3 \\ n_3 - 2n_3 n_1^2 & -2n_1 n_2 n_3 & n_1 - 2n_1 n_3^2 \\ -n_1 n_2^2 + n_1 n_3^2 & n_2 - n_2^3 + n_2 n_3^2 & -n_2^2 n_3 - n_3 + n_3^3 \\ -2n_1 n_2 n_3 & n_3 - 2n_3 n_2^2 & n_2 - 2n_2 n_3^2 \end{pmatrix}^{\mathbf{T}}. \tag{20}$$

The solution of $\mathbf{t}$ used by Michael (1984, 1987) is given by eq. (5)

$$\mathbf{t} = (\mathbf{A}^{\mathbf{T}}\mathbf{A})^{-1}\mathbf{A}^{\mathbf{T}}\mathbf{s}, \tag{21}$$

and the weighted LSQ from eq. (12) incorporates the weight matrix $\mathbf{W}$ and the solution for $\mathbf{t}$ is given by:

$$\mathbf{t} = (\mathbf{A}^{\mathbf{T}}\mathbf{W}\mathbf{A})^{-1}\mathbf{A}^{\mathbf{T}}\mathbf{W}\mathbf{s}. \tag{22}$$

For larger regions it is reasonable to invert for a set of tensors that are linearly dependent in space. Incorporating the weight matrix from eq. (12) into eq. (14) from Hardebeck & Michael (2006) results in weighted SATSI.

$$\mathbf{t}_a = (\mathbf{A}^{\mathbf{T}}\mathbf{W}\mathbf{A} + \epsilon^2\mathbf{D}^{\mathbf{T}}\mathbf{D})^{-1}\mathbf{A}^{\mathbf{T}}\mathbf{W}\mathbf{s}, \tag{23}$$

where $\mathbf{D}$ expresses the linear dependency of the neighboring stress tensors and ϵ is the dependency strength and $\mathbf{t}_a$ is the vector of all stress tensors.

$$\mathbf{t}_a = \begin{pmatrix} \mathbf{t}_1 \\ \mathbf{t}_2 \\ \vdots \\ \mathbf{t}_n \end{pmatrix}. \tag{24}$$

The STI routine by Michael (1984) is more applicable to smaller regions where the stress tensor can be assumed to be constant. SATSI relaxes this constraint by assuming that the stress tensor is constant within a subregion only, therefore, allowing STI to larger regions or tectonically more complex regions.

2.3 Confidence intervals

Hardebeck & Hauksson (2001a) stated that the uncertainty estimates of STI are not always properly represented. In particular, Hardebeck & Hauksson (2001a) showed that with increasing data size, the inversion by Michael (1984) tends to underestimate uncertainties. Since we focus on improving the underlying inversion routine by Michael (1984), the uncertainty estimates are compared between the weighted and unweighted inversions. We estimate uncertainties for both unweighted and weighted inversions on the same synthetic data sets. The correct stress tensor is considered to be inside the x per cent confidence region if its rotation angle to the best-fit stress tensor is smaller than $(100 - x)$ per cent of the bootstrapped stress tensor results. The rotation angle between two tensors is the Kagan angle, the smallest rotation angle between two three-axes systems (Kagan 1991). Ideally, the amount of correct stress tensors within the x per cent confidence region should be approximately x per cent. If the confidence regions are too large or too small, then the amount of correct stress tensors will be above or below x per cent.

3 DATA

This section examines the distribution of FMs and data with high leverage according to the model in eq. (15). Based on synthetic data, we demonstrate the ambiguity of stress tensor identification for outlier data of a catalogue with FM caused by two different stress

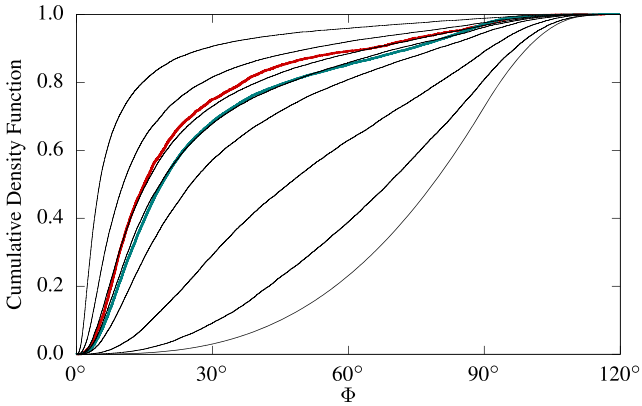

Figure 2. Cumulative DC rotational Cauchy distributions for different concentrations κ (grey lines, κ; from right to left: 1, 0.4, 0.2, 0.1, 0.07, 0.06, 0.04 and 0.02). The Kagan angle Φ, the smallest rotation angle between two FMs, follows this distribution. While rapidly increasing for small Φ, the distribution converges slowly to one for larger Φ—a typical behaviour of right-skewed distributions. Data following this distribution, therefore, have a relatively large number of outliers. The coloured curves represent empirical cumulative distribution functions (ECDF) of FM from GCMT for C 0.06) and the South American west coast (blue, $\kappa = 0.07$). The ECDFs are computed after Kagan (2013) for a reverse faulting events with maximum event distance of 50 km and a maximum event depth of 100 km.

tensors. We then introduce data-driven weighting based on ACE to reduce the impact of these ambiguous outlier data in the STI.

The data in this study are both real-world data and synthetic data. Real-world data are provided by the global centroid moment tensor (GCMT) catalogue (Dziewonski *et al.* 1981; Ekström *et al.* 2012). The FM data are declustered (Zaliapin *et al.* 2008; Zaliapin & Ben-Zion 2011) to investigate the background stress field and avoid effects of local stress changes due to major earthquakes. Declustering is also necessary to allow compatibility to the synthetic data, since these are generated under the assumption of event independence and a single stress tensor.

3.1 Synthetic catalogue generation

The catalogue with synthetic data is compiled with several boundary conditions. The basis for the catalogue is a stress tensor with principal stresses $S_1 > S_2 > S_3$. Because we are interested in stress orientations only, neither magnitudes nor the stress ratio R are explicitly defined and used here. In addition, we assume a Mohr–Coulomb criterion with an angle of internal friction of $\phi_\mathrm{f} = 30^\circ$ (Fig. 3a). The angle of internal friction is related to the coefficient of internal friction $\mu = \tan\phi_\mathrm{f}$. According to Byerlee (1978) a common value in natural materials is $\mu \approx 0.6$, which corresponds approximately to $\phi_\mathrm{f} = 30^\circ$. In an unfractured homogeneous medium, this scenario can lead to two possible fractures that are symmetrically aligned around the principal stress axes with fracture angle α (Fig. 3b). In case of the Mohr–Coulomb criterion for a newly formed fracture, the fracture angle α —as shown in Fig. 3(b)—and the angle of internal friction are related by (e.g. Zang & Stephansson 2010):

$$\alpha = \frac{\pi}{2} - \frac{\phi_\mathrm{f}}{2}. \tag{25}$$

Both slip and normal vectors on the two conjugate fracture planes form the reference events for the generation of the synthetic catalogue. The usage of two events (slip vectors) in conjunction with the Mohr–Coulomb criterion for newly formed fractures (represented

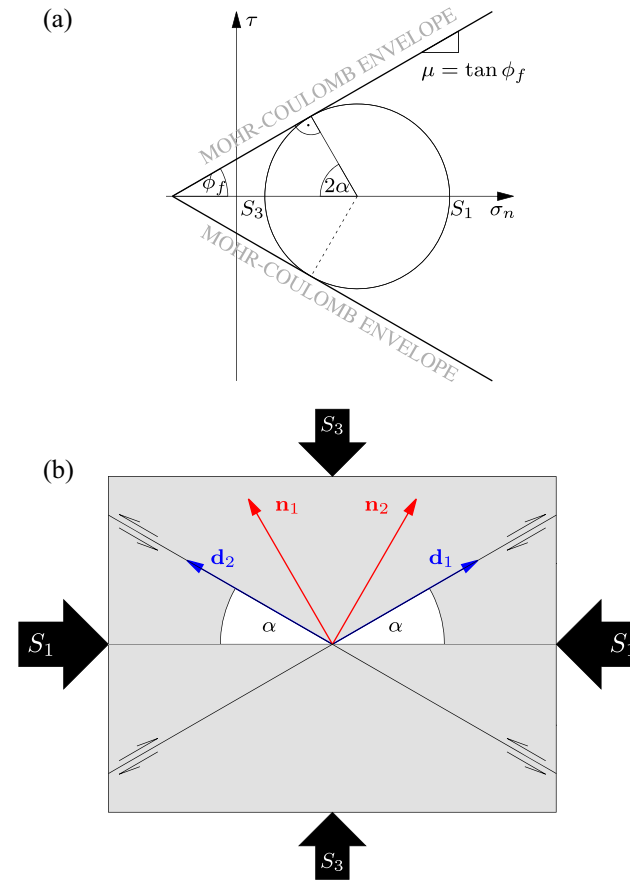

Figure 3. (a) Mohr diagram for the Mohr–Coulomb failure criterion. The Mohr–Coulomb failure criterion is of form $\tau = C + \sigma_\mathrm{n} \tan\phi_\mathrm{f}$, where σ_n is the normal stress, τ the shear stress, C the cohesion (offset at $\sigma_\mathrm{n} = 0$) and $\mu = \tan\phi_\mathrm{f}$ the coefficient (angle) of internal friction. Furthermore, α is the fracture angle, S_1 the maximum and S_3 the minimum principal stress. For simplicity we do not show the intermediate principal stress S_2. Failure occurs where the Mohr circle reaches the failure envelope. The upper and lower envelopes relate to the conjugate fault planes as shown in panel (b). (b) Setting of the reference events for the generation of the synthetic catalogue. The reference events originate as fractures in a homogenuous, unfractured medium. We consider a Mohr–Coulomb fracture criterion with a fracture angle $\phi_f = 30^\circ$. As in (a) S_1 is the maximum and S_3 the minimum principal stress. The intermediate principal stress S_2 is perpendicular to the S_1–S_3-plane. The fracture planes are described by the normal vector $\mathbf{n}_i$ and the slip with $\mathbf{d}_i$. Since both fractures are equally likely to occur as a result of the given stress conditions and friction angle, both are used as reference events equally. In addition, only with both conjugate fractures are the principal stress orientations of the stress tensor unambiguously represented by the slip orientations.

by normal vectors) provides a one-to-one correspondence to the stress tensor, as a single event may not fully constrain the stress tensor (McKenzie 1969). However, the magnitude of the slip is usually unknown and thus the full stress tensor cannot be inferred. Thus, given the definition of the STI of Michael (1984) in Section 2.2 based on unit slip vectors, the two unit slip vectors—on faults related to each other by the Mohr–Coulomb fracture criterion—are sufficient to uniquely constrain the principal stress orientations of the deviatoric stress tensor **t**.

We assume the Wallace–Bott hypothesis for the slip orientation, that is, the slip is parallel to the maximum resolved shear stress. For the reference events, this results in an orientation of the slip and

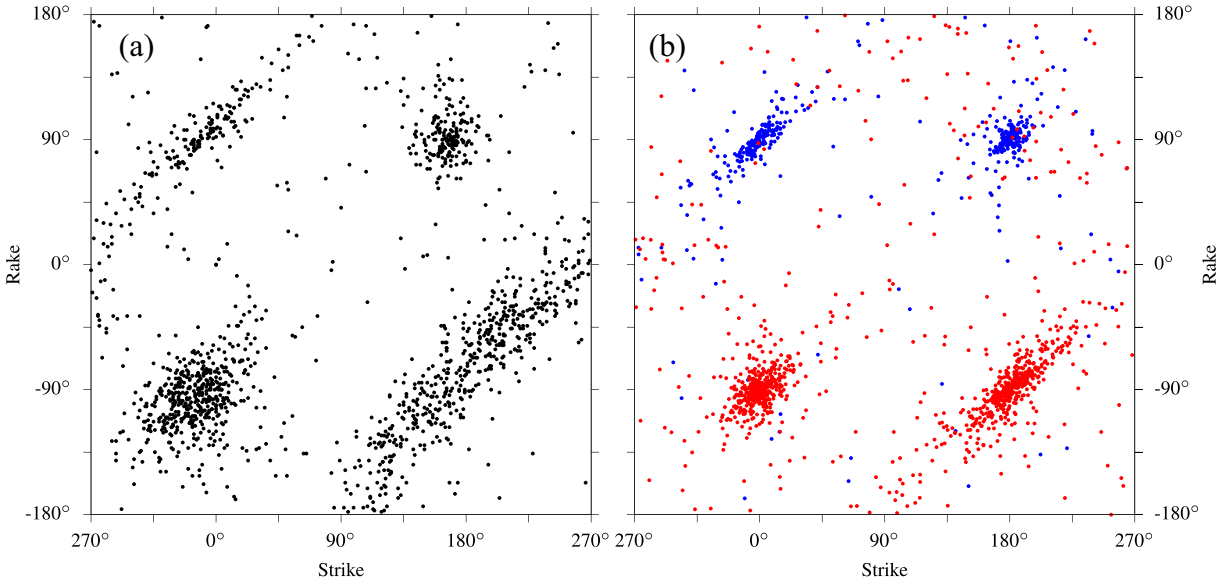

Figure 4. (a) FM data from northern Chile in the strike-rake plane. The four notable clusters represent the two nodal planes for reverse faulting events (positive rakes) at the plate interface and normal faulting events (negative rakes) within the slab. (b) Synthetic FM data sampled from two DC rotational Cauchy distributions with different stress tensors: reverse faulting (blue, $\kappa = 0.0625$) and normal faulting (red, $\kappa = 0.125$). Although only based on the DC rotational Cauchy distribution and therefore only on stress orientations and no stress magnitudes, synthetic data yield a high similarity to the real data. The synthetic data show that each tensor can cause FM with virtually all strikes and rakes. Data following the heavy tailed DC rotational Cauchy distribution have a non-negligible number of severe outliers. Though the synthetic catalog is based on two reference events, only FM associated with the eastward dipping fault plane are shown.

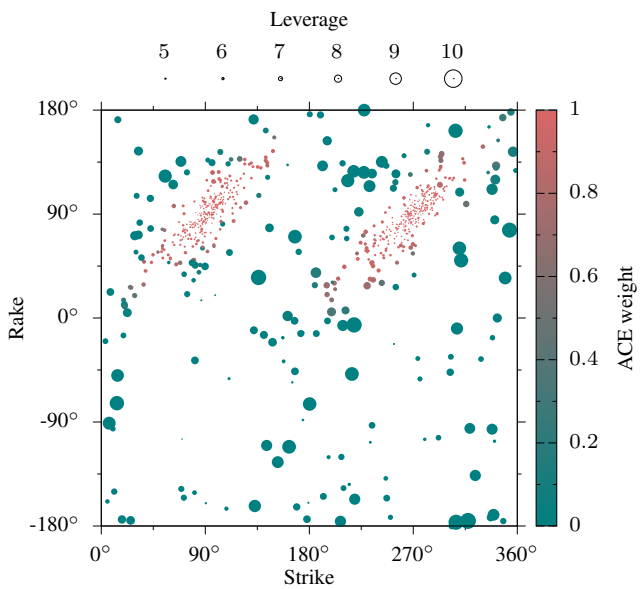

Figure 5. Leverage in the STI after Michael (1984) for a synthetic data set of FM drawn from DC rotational Cauchy distribution of a stress tensor associated with reverse faulting. While leverage is smallest in the two clusters for either nodal plane, leverage increases with distance to the clusters. The ACE-based weights of this data set are indicated by colour. The high-leverage data are all down-weighted to an extent that their impact is negligible in the STI.

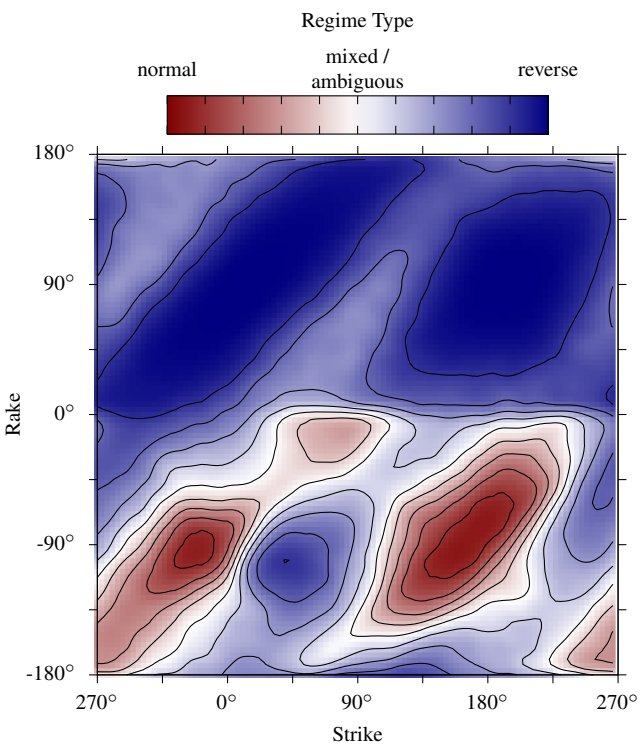

Figure 6. Relative stress tensor prevalence in synthetic FM data similar to shallow seismicity of the upper 50 km in the Chile data with 80 per cent reverse and 20 per cent normal faulting with clusters similar to those from Fig. 4. Though normal faulting events are less common, in the regions off the cluster centres (pure blue and red regions), data of the extensional stress tensor may occur as reverse faulting events to such an extent that stress tensor assignment becomes ambiguous even for reverse faulting (less colour saturated parts).

normal vectors in the S_1–S_3-plane. The null axis (the cross product of the slip and normal vector) is oriented parallel to S_2. No formal differentiation between the formation of a new fracture and the reactivation of a pre-existing fault is considered for the catalogue, that is, any event may represent either case.

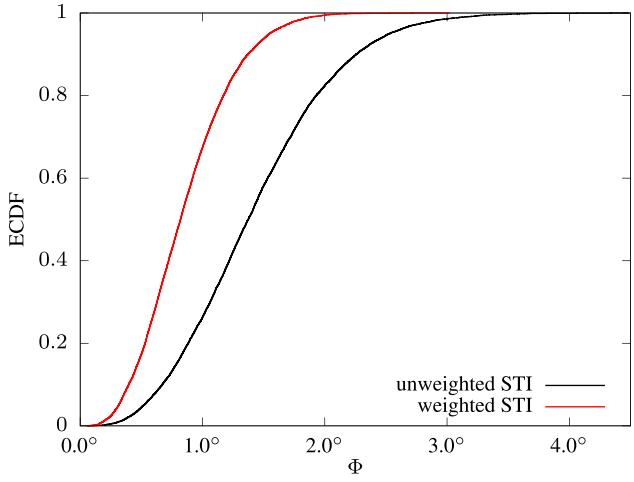

Figure 7. ECDF of the rotation angle between the stress axes of the inversion and the reference values of the synthetic catalogues. In total 20 000 synthetic FM catalogues were sampled from the DC rotational Cauchy distribution and inverted for the stress orientations with and without weights. The distributions show, that the rotation angles of the unweighted STI (black) are on average 40 per cent larger than for the weighted STI (red). Though 15 per cent of the data are downweighted such that they are effectively removed from the data set, the weighted STI results in 40 per cent reduced error in comparison to the unweighted STI.

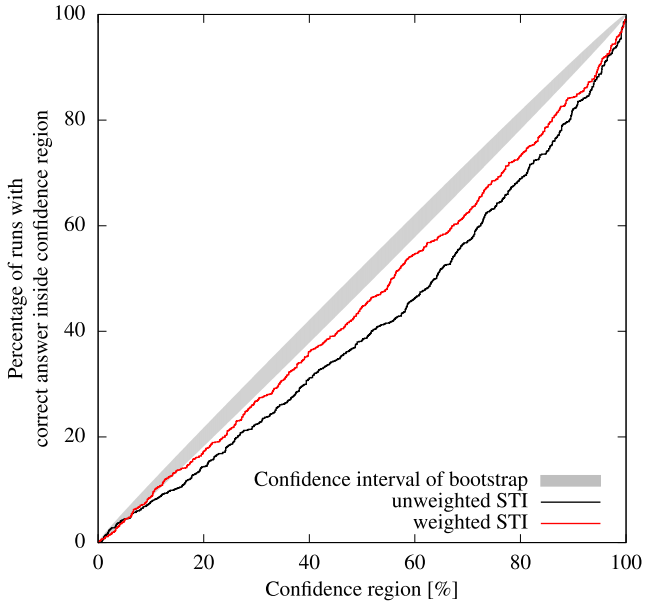

Figure 8. Confidence region appropriateness for both weighted and unweighted STI after Hardebeck & Hauksson (2001a). The amount of correct stress tensors within the x per cent confidence region is plotted as a function of x. If the confidence regions are appropriate, the amount of correct stress tensors falls in the grey area. Results from an experiment with perfect confidence regions would have a 95 per cent probability of falling within the grey zone, which is the 95 per cent confidence interval of the binomial probability distribution for 2000 trials with an x per cent probability of success each trial. As reported by Hardebeck & Hauksson (2001a), the uncertainties of STI after Michael (1984) for larger data sets are underestimated. However, the unweighted STI (black) underestimates uncertainties more than the weighted STI (red). This implies that the relative uncertainty reduction between both STIs of 40 per cent shown in Fig. 7 is larger, that is, the weighting improves results by more than 40 per cent.

To build the catalogue, randomizations are applied to the two reference events. The randomization is introduced as rotation angles of the FMs. The rotation angle follows a double-couple (DC) rotational Cauchy distribution (Kagan 1992, 2013) and implies two assumptions:

(1) Variations in the rupture surfaces of earthquakes, as the surfaces may not be completely planar (Kagan & Knopoff 1985; Kagan 1990).
(2) The existence of random stresses due to unavoidable defects in the medium, preventing rupture surfaces from having the same orientation (Kagan 1990).

The orientation of FM from a constant background stress tensor and the differences between FM pairs have been extensively studied and the DC rotational Cauchy distribution has been shown to adequately describe the distribution of FM orientations (Kagan 1992, 2007, 2013). This distribution is characterized by a single parameter, the concentration κ, which determines the spread of the distribution. Examples of the DC rotational Cauchy distribution for different κ are shown in Fig. 2. The difference between two FM stated in NDB-axes (i.e. axes parallel to fault normal vector, the slip vector and the null vector [orthogonal to the former two]) is expressed as the Kagan angle.

The randomization of the two reference events is applied in two steps. For each event in the synthetic catalog, we sample a Kagan angle from the DC rotational Cauchy distribution. In a second step, a rotation axis from a uniform distribution is sampled. The NDB-axes of the reference event are rotated around the rotation axis by the Kagan angle. For the first half of the catalog, we use the first reference event, for the second half, the second reference event.

The variability added by the DC rotational Cauchy distribution is only related to stress in a medium with random defects (Kagan 1992). Effects of FM errors on stress inversions have been investigated by Hardebeck & Hauksson (2001a) and the distribution of FM errors in terms of the Kagan angle follows a von Mises-Fisher distribution (Kagan 1992, 2000, 2013). The variability due to random defects considered in this study is much larger than the variability introduced by FM uncertainties (Kagan 2000) and FM uncertainties are not further considered.

Kagan (1992) and the subsequent studies investigated the distribution of rotation angle between pairs of FM without respect to a reference event. The Cauchy distribution and its derived distributions belong to the group of stable distributions (Kagan 2000). A distribution is stable if a linear combination of independent random variables with that distribution results in the same distribution, only with a change of parameters. This property is also known infinite divisibilty. The scale (concentration) of the Cauchy distribution and its derivates is the linear combination of the individual scales (concentrations) of the individual Cauchy distributions. Since all samples in our catalogues are independently drawn from the same DC rotational Cauchy distribution, the distribution of all pairs follows again a DC rotational Cauchy distribution. The rotation angle between some events A and B can be seen as linear combination of the rotation between A and C, and a rotation between B and C. Event C is any other event, for example, the reference event. It follows that for all pairs of FMs the DC rotational Cauchy distribution has its concentration doubled from the sampling distribution.

The introduction of a random component from the DC rotational Cauchy distribution results in a discrepancy to the Wallace–Bott hypothesis. However, Lisle (2013) investigated how strictly

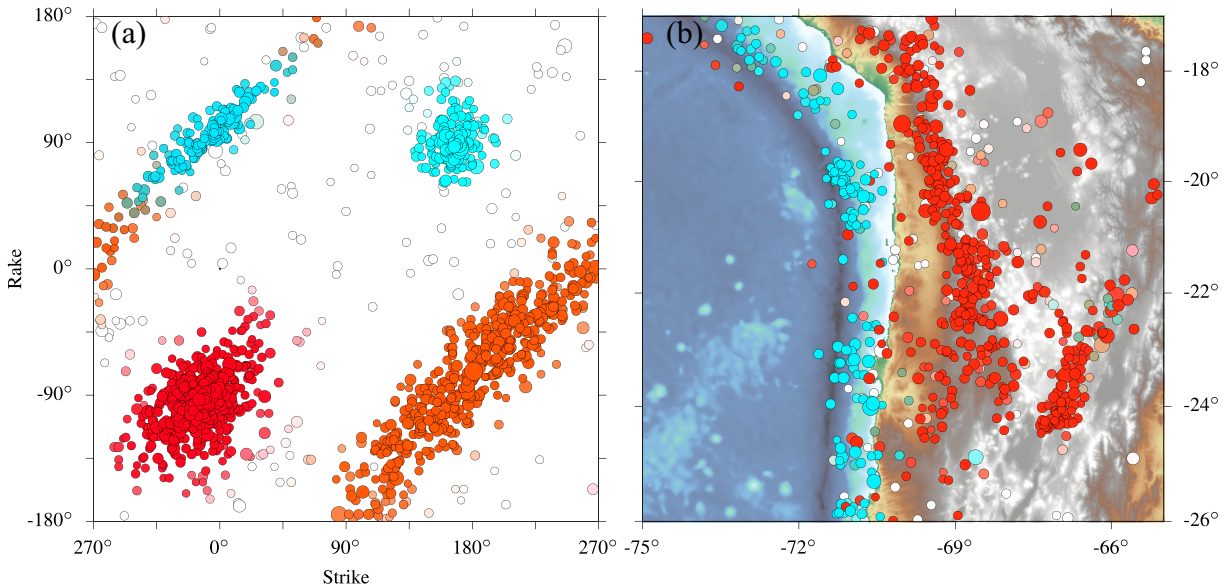

Figure 9. (a) Strike-rake plot of GCMT FMs (both nodal planes) from northern Chile between 1976 and 2017 (26°S–17°S, 75°W–65°W). Clusters were identified with ACE with colour saturation according to the probability of belonging to that cluster (cyan—plate interface,reverse faulting; red—intraslab, normal faulting; white—unclassified). The probabilities of the plate interface clusters correspond to the weights used in the weighted STI. The strike axis of the plot has been shifted by 90° to show all clusters continuously. (b) Map of epicentres of GCMT FMs in panel (a). Colour scheme is identical to part (a). Since one FM consists of two nodal planes, the colour for the epicentre is based on the average weight of both nodal planes. Most reverse events (cyan) are close to the trench and are associated with the plate interface, while normal faulting events (red) are further to the east and are associated with the subducted slab.

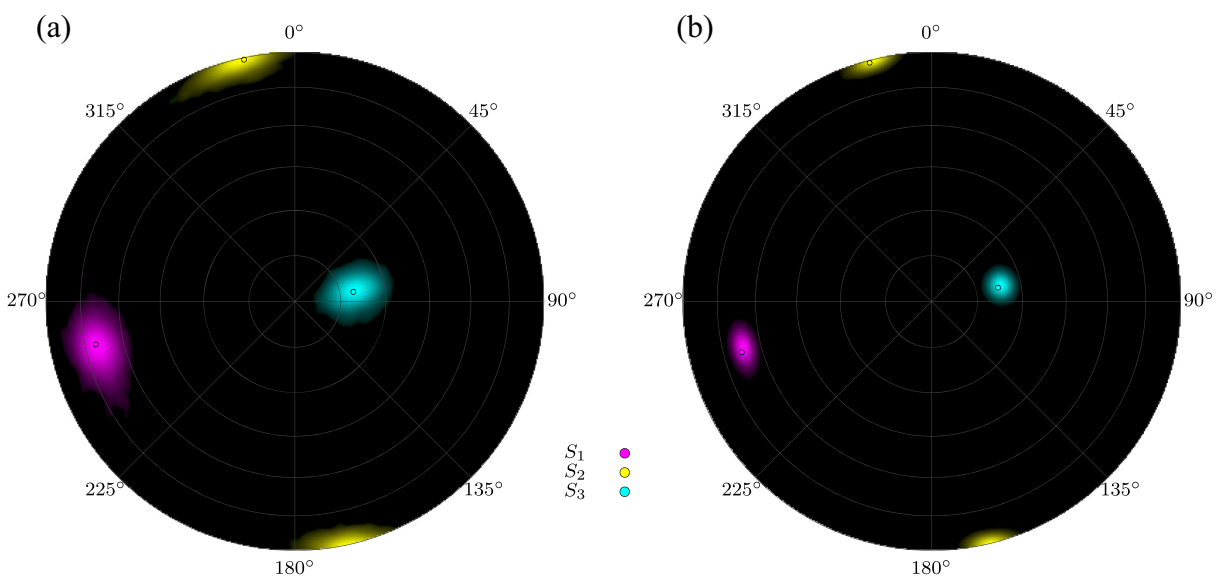

Figure 10. STI for northern Chile: (a) unweighted; (b) weighted. Principal stress axes are shown by small circles, uncertainty distributions by coloured areas. Though only 15 per cent of the data are effectively removed (with near zero weights), uncertainties decrease by a larger margin.

the Wallace–Bott hypothesis should be observed. Lisle (2013) remarked, that the resolved shear stress oriented ≈26° off the orientation is at 90 per cent of the maximum resolved stress. This implies a range of 52° over which the shear stress varies only by 10 per cent and it has been pointed out that such variability should be considered in STI. The DC rotational Cauchy distribution is densest around its mean and has a relatively large positive skew if κ is sufficiently small, that is, most applied rotations are only a few degrees. With only small rotations applied, the majority of the events in the synthetic catalogue still closely approximates the Wallace–Bott hypothesis.

3.2 Data distribution

One common assumption for the STI is that all data are caused by the same stress tensor (Maury *et al.* 2013). When considering real-world data, several stress tensors might be present even on smaller scales. Fig. 4(a) shows FM data from northern Chile and in comparison synthetic FM data are shown from a stress tensor corresponding to reverse and normal faulting, respectively. The distribution of random samples from the DC rotational Cauchy distribution is very similar to real-world data (e.g. Kagan 1992, 2013). In both cases

Table 1. Principal stress orientations for northern Chile of the conventional and weighted STI. Orientations are given as trend (tr.) and plunge (pl.) and uncertainties (one standard deviation) in italics below.

	Conventional		Weighted STI	
	tr.	pl.	tr.	pl.
S_1	256.7	19.8	256.1	23.1
	4.0	*3.6*	*1.9*	*1.2*
S_2	347.1	1.1	346.3	0.4
	3.6	*2.6*	*1.6*	*1.5*
S_3	80.4	70.0	77.1	66.9
	7.2	*3.6*	*3.3*	*1.2*

data form dense clusters, but a significant number of outliers is also present.

Two different stress regimes prevail in Chile (and by extension most of South American west coast) (e.g. Pardo *et al.* 2002). At the plate boundary interface stresses result mostly in reverse faulting, while within the subducting slab stresses lead to normal faulting FM. The transition between the two regimes is continuous in space and additionally not well-constrained due to FM hypocentre uncertainties.

When sampling from the DC rotational Cauchy distribution from two different stress tensors, we know which random datum originates from which stress tensor. This knowledge is unavailable for real-world data and thus the synthetic data allows insight into its composition (Fig. 4b). While the dense clusters are dominated by FM of one stress tensor, the outlying data are composed of FMs of both stress tensors. This stress tensor overlap in the outlying regions limits the demand for FM diversity in STI, as a clear stress tensor assignment for real data is not feasible.

This limitation is even present if FM of one of the two stress tensors are less frequent. The synthetic catalogue, which is the basis for Fig. 6, contains 80 per cent reverse and 20 per cent normal faulting events. Still, regions off the cluster centres (shown by dots for either nodal plane and tensor type) are equally likely to contain FM from either tensor. Therefore, a clear distinction of tensors for those FM can neither be achieved from location alone nor from the FM in every case. The compiled FM catalogue for the STI will be most likely polluted by data of different stress tensors—especially in the outliers. If the presence of a single stress tensor is not given, it is necessary to downweight those FM that cannot be assigned to a particular stress tensor. This inadvertently reduces the data size of the outliers and thus the data variability, which has been shown to reduce the bias of STI (Hardebeck & Hauksson 2001b). However, if the outliers originate from another stress tensor, increased data variability may not result in a decreased bias.

3.3 Data leverage

As introduced in Section 2.1, the leverage states how much an observed datum contributes to its own prediction. An example of the leverage of the inversion routine by Michael (1984) is shown in Fig. 5 for a synthetic data set of FM from a stress tensor with S_1 horizontally oriented and S_3 vertically, resulting predominantly in reverse faulting. The calculation of the leverage is similar to the STI routine as bootstrapping is applied to randomly select one nodal plane as the auxiliary plane. The final leverage is the average of all leverage calculations of the resampled data.

The distribution of the leverage follows approximately inversely the data density (Fig. 5). The less data are realized for a certain FM type, the higher the leverage, that is, leverage increases with distance to the average FM. Thus, outliers are usually also high-leverage data.

In the previous section, we have shown that outliers cannot be assigned to a specific tensor in every case. However, the STI will give by design those ambiguous data a higher weighting due to their higher leverage. This contradicts the basic assumption that less reliable data should be down-weighted instead of up-weighted. Even if all data arose under a single stress tensor, an outlying datum will have a larger impact on the outcome then a datum that is close to the average.

3.4 Data weighting

In Section 2.2, the weight matrix **W** has been introduced into STI (eq. 22). The weights we use are derived by ACE (Specht *et al.* 2017). In Section 2, we demonstrated that the inversion tends to be more sensitive to outlying data which can be ambiguous in terms of stress tensor assignment which is crucial for data selection for STI.

The algorithm for ACE requires the same input as STI: FM data. Expectation-maximization (Dempster *et al.* 1977) is a widely used soft (fuzzy) clustering routine. Each FM is represented by two sets of angles (strike, rake and dip), each for one nodal plane. These angles are used to estimate probability distributions which describe the clusters of nodal planes. The functions are also called component distributions and the full set of the distributions form the mixture distribution. A cluster of nodal planes may be represented by a single component or several, depending on the shape complexity of the cluster. Each FM has a certain probability to belong to each distribution and thus to each cluster.

The values of the distributions are directly used as weights in the weight matrix of eqs (22) and (23) (Specht *et al.* 2017). The clusters identified by ACE and described by the distributions can be associated with a stress tensor (e.g. at a plate interface). FM data not associated with any cluster remain unclassified. Unclassified data can be associated with data of increased leverage in the inversion (Fig. 5). If more than one stress tensor is present, the unclassified data fall into regions where stress tensor assignment is mixed/ambiguous (Fig. 6). It is only in the presence of several stress tensors necessary that the weights provided by ACE are used. If ACE identifies only FM clusters associated with, for example, reverse faulting at an interface, then the data weighting is not necessary as no ambiguities arise. Accordingly, ACE can also be used to determine, whether data weighting for STI is required.

3.5 Synthetic data test

We test the performance of both the unweighted and weighted STI routine on synthetic catalogues with known parameters. The synthetics are based on the DC rotational Cauchy distribution.

The synthetic catalogue is a sample of events drawn from a DC rotational Cauchy distribution with $\kappa = 0.06$ and the reference events are a pure reverse faulting events. The reference nodal planes have rakes of 90°, the strikes are 90° and 270° and dips are 30° and 60°. Most of the random events drawn from the DC rotational Cauchy distribution are distributed closely around the reference events. To estimate the differences between the unweighted and weighted STI results, we generated 10 000 synthetic catalogues each with 800 events. An example of such a catalogue is shown in Fig. 4(b). For each catalogue both types of STI were performed—unweighted and weighted—with weights determined by ACE for each catalogue.

Table 2. Principal stress orientations for the seven regions of western South America as in Fig. 12 of the unweighted and weighted STI. Orientations are given as trend (tr.) and plunge (pl.) and uncertainties (one standard deviation) in italics below.

Region	Unweighted STI						Weighted STI					
	S_1		S_2		S_3		S_1		S_2		S_3	
	tr.	pl.	tr.	pl.	tr.	pl.	tr.	pl.	tr.	pl.	tr.	pl.
1	260.3	11.4	351.7	6.9	112.1	76.4	259.8	19.7	350.2	1.0	83.1	70.3
	1.8	*2.0*	*1.8*	*2.6*	*10.6*	*2.2*	*1.0*	*0.6*	*0.9*	*0.7*	*1.8*	*0.6*
2	261.4	10.2	352.6	6.5	114.4	77.7	260.9	19.8	351.1	0.5	82.5	70.2
	1.6	*1.8*	*1.7*	*2.4*	*10.6*	*2.0*	*1.0*	*0.6*	*0.9*	*0.7*	*1.8*	*0.6*
3	257.5	15.1	350.2	9.8	111.6	71.7	259.0	19.6	349.6	1.6	84.0	70.3
	1.8	*2.0*	*1.9*	*3.0*	*8.5*	*2.4*	*1.2*	*0.6*	*1.0*	*0.8*	*2.1*	*0.6*
4	263.2	12.2	353.6	1.7	91.6	77.6	263.5	19.8	173.0	1.2	79.9	70.1
	1.3	*1.6*	*1.3*	*1.6*	*7.5*	*1.6*	*1.0*	*0.6*	*0.9*	*0.6*	*1.7*	*0.6*
5	263.0	16.1	354.3	4.3	98.8	73.1	263.5	19.7	173.2	0.7	81.4	70.2
	1.6	*2.0*	*1.7*	*2.5*	*8.5*	*2.1*	*1.1*	*0.6*	*1.0*	*0.7*	*2.0*	*0.6*
6	262.9	15.6	353.3	1.5	88.4	74.2	266.1	19.7	175.6	1.6	81.0	70.2
	1.2	*1.7*	*1.2*	*1.8*	*6.6*	*1.8*	*0.9*	*0.6*	*0.8*	*0.6*	*1.5*	*0.6*
7	262.7	20.1	354.4	4.4	96.0	69.2	266.4	19.8	176.0	1.3	82.4	70.1
	1.4	*2.2*	*1.5*	*2.4*	*6.6*	*2.3*	*0.9*	*0.5*	*0.8*	*0.6*	*1.6*	*0.5*

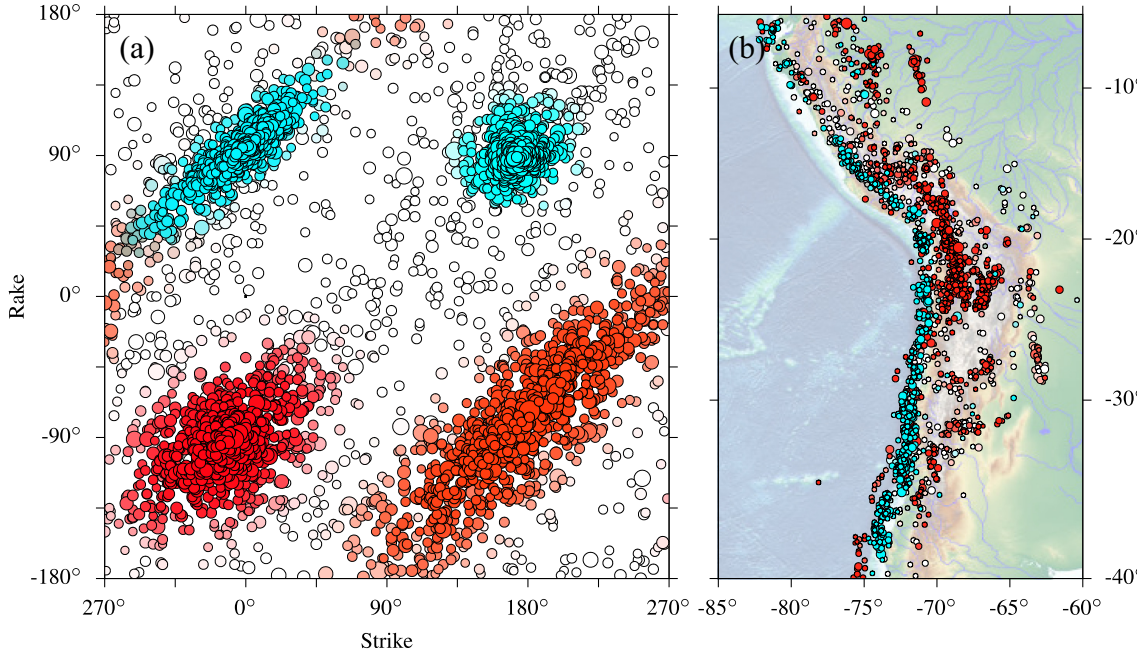

Figure 11. Same as Fig. 9, but for FM data from the South American coast between 1976 and 2017 (40°S–5°S, 80°W–60°W). Even though the region (b) has a much larger extent then northern Chile example, the identified clusters are similar to those of northern Chile.

The distribution of rotation angles of inverted stress orientations with respect to the stress orientation of the reference event indicate a reduction of 40 per cent in uncertainties, while only 15 per cent of FM data has been down-weighted to an extent that the data are effectively removed from the data set. The removed/down-weighted data show comparatively large residuals, while data in the bulk remain unchanged. The data leverage shows that the removed data have an above average influence on the model result. Due to the removal of these high-leverage outlying data, the obtained stress tensor orientations are more robust, that is, orientations are not affected but uncertainties are reduced.

The appropriateness of the uncertainty estimates for both weighted and unweighted STI are shown in Fig. 8. As found by Hardebeck & Hauksson (2001a), the uncertainty estimates of STI after Michael (1984) are too small for both weighted and unweighted routines. However, the weighted STI underestimates uncertainties to a lesser degree than the unweighted STI. The aforementioned relative uncertainty reduction of 40 per cent is therefore larger for when accounting for the different degrees of underestimation.

4 EXAMPLES

In this section, we present two case studies from South America. The first example is from northern Chile where in 2014 the Iquique earthquake occurred and the second example covers the entire west coast of South America. The FM data are from the GCMT catalogue (Dziewonski *et al.* 1981; Ekström *et al.* 2012) from 1976 to 2017. FM clusters are identified with ACE and the probabilities of each event are used as weights in the weighted STI. We invert for stress tensor orientations with and without weights. For the STI and the derivation of the weights we use declustered catalogues (Zaliapin *et al.* 2008). Uncertainties are estimated by bootstrapping the data

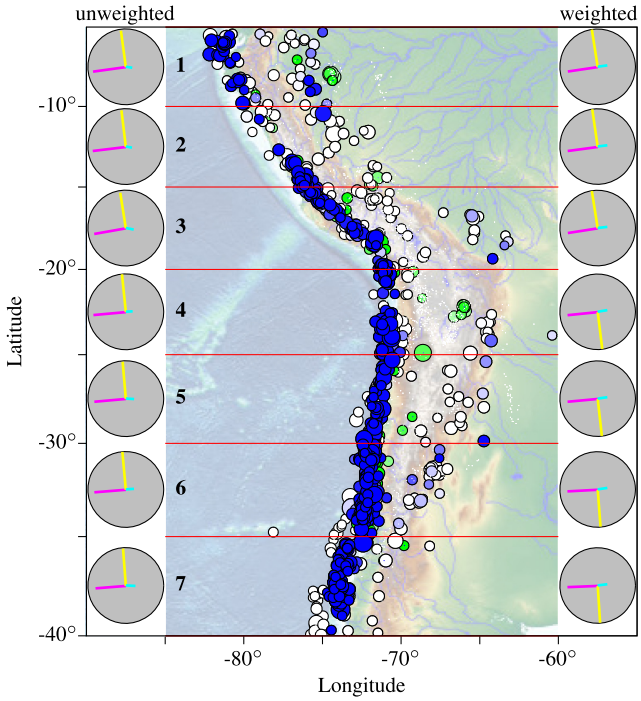

Figure 12. Subdivision of western South America for SATSI in regions 1–7 (red lines). Events in the map are used in both STI: All events shown have either an ACE weight ≥0.5 or have a depth of ≤50 km. Colour saturation corresponds to ACE weights for plate interface events (colour saturation is equivalent to the average saturation of the two plate interface/reverse faulting cluster in Fig. 11). Events in blue and white have a depth of ≤50 km and are used in the unweighted STI; events in blue and green are used in the weighted STI. Green events have an ACE weight of ≥0.5 and a depth of >50 km. In the weighted inversion all events are included, but events with weights below 0.5 are not shown in the figure. Principal stress orientations for each region are shown on either side of the map for unweighted (left) and weighted (right) STI. The S_2 orientations (yellow) fluctuate between north and south and the right-hand column which is due to the usage of the lower hemispheric projection; all S_2 orientations are almost identical with near horizontal plunge and a north-south trend. Principal stress orientations are given in Table 2.

10 000 times and, following Michael (1987), by randomly selecting nodal planes as rupture and auxiliary planes, respectively.

4.1 Northern Chile

Seismicity in northern Chile is dominated by plate interface and intraslab earthquakes. In the region considered here (26°S–17°S, 75°W–65°W) plate interface activity is mostly confined to the upper 50 km close to the coast, while most intraslab activity is below that depth. Crustal activity to the east of the coast is associated with orogenic processes. The catalogue contains 736 events after declustering.

In the unweighted estimation of the stress tensor at the plate interface, we only included events shallower than 50 km of the entire region (174 events). Results (Fig. 10a) indicate that S_1-direction is westward, parallel to the movement orientation of the Nazca plate with respect to the South American plate (Bird 2003), and dipping with appr. 20°. Uncertainties are represented in a Kernel density estimate with a von Mises-Fisher kernel.

For the weighted STI we apply ACE for the declustered GCMT catalogue of northern Chile with 736 events without any additional *a priori* information about the FM. Four clusters are identified (Fig. 9). Two of each (for either nodal plane) are associated with normal (intraslab) and reverse faulting (plate interface), respectively. The unclassified events are mostly near the surface and are associated with thrusting in the Andes. The weights are based on the probabilities of the two clusters associated with plate interface activity. The sum of the weights expressed as fractions is 19.4 per cent for plate interface, 65.4 per cent for intraslab and 15.2 per cent for unclassified. With respect to the total number of FM (736), 19.4 per cent is equivalent to 143 events which is comparable to the 174 events considered in the unweighted STI.

The three principal stress orientations differ only by a rotation angle of 3.9° between the unweighted and weighted STI. Differences are more prominent in the plunge than in the trend. In all cases uncertainties of the weighted STI estimates are reduced significantly (Table 1).

4.2 Nazca plate

The second example covers the portion of the South American west coast between 40°S and 5°S. The longitudinal extent includes all major seismicity in the latitude range (85°W–65°W, Fig. 11b). The catalogue of northern Chile in the first example is a subset of this data set, thus similar results for normal and reverse faulting are expected.

STI in this example is based on SATSI (eq. 23) and focuses on plate interface activity with a maximum depth of 50 km. The region is subdivided between −85° and −60° longitude into seven stripes of 5° width between latitudes −40° and −5° (Fig. 12). SATSI is performed without weighting and with ACE-based weights. The dependency in eq. (23) is set in both cases to $\epsilon = 0.2$.

The catalogue for this region contains 1941 events and the set-up for ACE is as in the previous example. Four clusters similar to those found for northern Chile are identified: two for reverse and normal faulting, respectively (Fig. 11). Remaining data are unclassified. The clusters for normal and reverse faulting are similar in shape and location to the clusters from northern Chile. This similarity suggests that plate interface rupture processes are similar along the west coast of South America. The number of events per event type differs from northern Chile, as the sum of weights indicates 28.9 per cent as plate interface, 38 per cent as intraslab and 33.1 per cent as unclassified. As in the case for northern Chile, only data with a depth of less than 50 km are used in unweighted STI (827 events). With 28.9 per cent of 1941 events weighted as plate interface results in 560 events for the weighted STI.

In Fig. 12, inversion results are shown for each for the unweighted (left-hand column) and weighted inversions (right-hand column). Principal stress orientations are similar to each other, with S_1 oriented westward, S_2 oriented northward (southward), and S_3 oriented downward and slightly eastward. S_2 orientations of the unweighted inversion are more tilted than orientations derived from the weighted inversion. All S_2 orientations are from the unweighted approach are northward, while in the weighted case the orientation flips between north and south, indicating that S_2 orientations are nearly horizontal (Fig. 12, right-hand column).

Principal stress orientations with their uncertainties for both SATSI inversions are shown in Fig. 13 (a, unweighted; b, weighted). Individual solutions are shown by different shades of hue, with S_1 in red/purple, S_2 in orange/green and S_3 in green/blue. The differences of principal stress orientations for all regions of the weighted and unweighted STI range between 4.7° and 10.8°. Trends and plunges

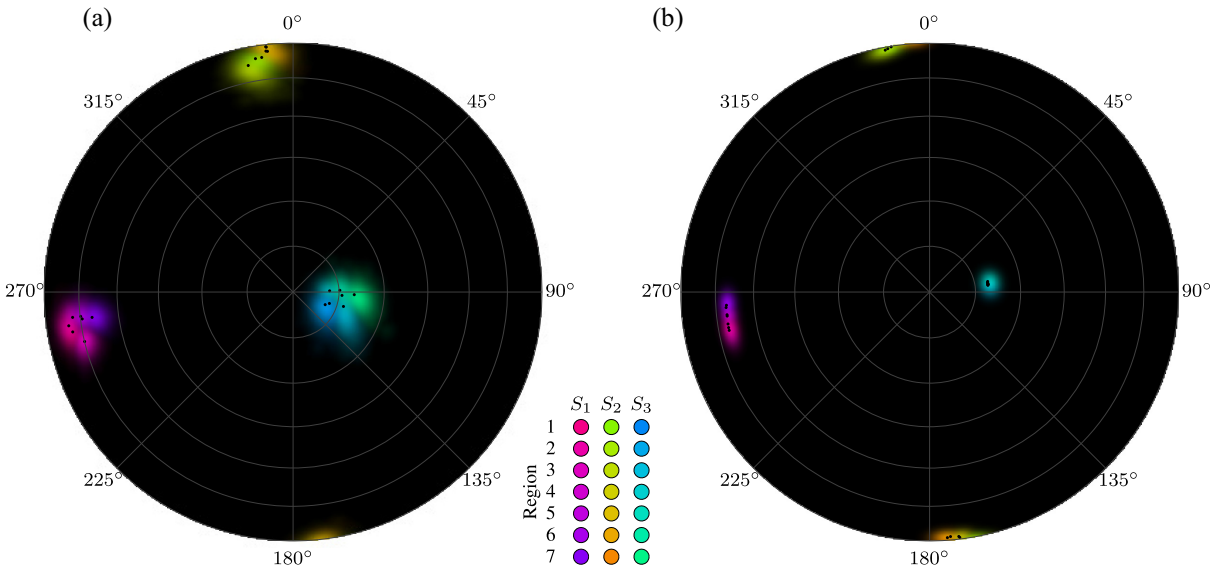

Figure 13. Principal stress orientations with SATSI (a, unweighted; b, weighted) for the South American coast (Fig. 12). Principal stress orientations are all over similar to those of Northern Chile (Fig. 10). The results of the unweighted STI not only show larger uncertainties per region (densities with same hue) to the weighted STI, but also between regions principal stress orientations are more diverse than those obtained from the weighted STI.

and their respective uncertainties for all seven regions are summarized in Table 2. In case of the weighted inversion (Fig. 13b), uncertainties for each stress tensor are larger than the variance of the principal stress orientations for all regions, that is, the results for each region are consistent with each other. In the unweighted STI, principal stress orientations of all regions are more scattered than in the weighted case. This difference of scattering is best illustrated in the orientations of S_3: While all bins in the weighted estimate have near identical S_3-orientations (Fig. 13b, blue/green region in the centre), S_3-orientations of the unweighted estimates are diverse to a level that they are mostly separate even with their uncertainties (Table 2). The orientation of S_1 of the unweighted inversion follows a horseshoe pattern (Fig. 13a, left) while in the weighted STI orientations are at a constant plunge. This horseshoe pattern is most likely caused by outlying data, as these are not identically distributed for each region due to the high variability in the occurrence of such more rare events. The rarity of these events is compensated in the STI by the increased leverage.

5 DISCUSSION AND CONCLUSION

The compilation of an FM catalogue for STI that strictly follows the assumptions of the stress inversion routine cannot be achieved by spatial and deterministic selection alone. We demonstrated that STI can be improved by applying data weighting based on ACE. Since the weights are not fully dependent of the event's hypocentre, they add an additional constraint to the otherwise purely spatially constrained extent of the data for the final catalogue. Furthermore, the weights are derived in a data-driven way, thus reducing effects from expert elicitation in the case of selecting spatial bins. Due to the complexity of the FM distribution in the Earth, it is necessary to identify and remove/down-weight outliers if FM data originates from several stress tensors. The weighting not only improves the stress tensor solutions but also reduces uncertainties.

Outliers increase inadvertently data diversity, which has been shown by Hardebeck & Hauksson (2001b) and is required for less biased stress tensor estimates. Outliers can originate either from different stress tensors or are extreme cases of the dominant stress tensor. However, the former case needs to be avoided from a physical point of view, the latter because these extreme value data influence the outcome of the inversion more than the close to average data. The fewer data are used in an inversion, the larger the range of leverage. Under the assumption that angles between FM follow a DC rotational Cauchy distribution, FM outliers can occur at higher frequencies than expected from a normal distribution. A clear separation of both cases is not possible when two different stress tensors are in proximity to each other. Therefore, the reasons for the differences of stress orientations from weighted and unweighted STI in the examples cannot be resolved as well.

Data selection in unweighted STI is highly dependent on the hypocentre location. However, the hypocentres are not always a good proxy whether events belong to a single stress tensor or not. Data weighting based on the distribution of the FM angles, as given by ACE, allows data selection independent of the hypocentres. The data selection is not only subject to the hypocentres but also to the properties of the focal mechanisms. Thus, STI is less sensitive to the spatial binning.

A major advantage of data weights is their implementation into any of the existing methods, as has been exemplified by the seamless incorporation of weights into the STI routine of Michael (1984) and Hardebeck & Michael (2006). The underlying routines remain unchanged and results have been shown to be consistent. However, uncertainties are considerably reduced by discarding only a small portion of the data set. ACE can also be used to determine whether data weighting is necessary, depending on the identified clusters. If the identified clusters are associated with multiple stress tensors (e.g. at a plate interface or in a subducting slab), then weighting is recommended. Furthermore, other types of data weighting can be added by expanding the weight matrix, for example, by incorporating data uncertainties as in Armijo *et al.* (1982).

Data weighting can also be incorporated into more advanced methodologies for STI (e.g. Martínez-Garzón *et al.* 2016). As such, data-driven methods not only allow a refined analysis of the stress

field but also open up other fields in stress field research, for example, stress transients. Here, the reduction of uncertainties of stress tensor estimates is a necessary prerequisite for investigation of the spatio-temporal variability of the stress field.

ACKNOWLEDGEMENTS

FM data are accessible at http://www.globalcmt.org/ (GCMT, Dziewonski *et al.* 1981; Ekström *et al.* 2012). Stress tensors according to eqs (22) and (23) were computed with the Armadillo library for C++ (http://arma.sourceforge.net/) (Sanderson & Curtin 2016). Maps are generated with GMT (Wessel *et al.* 2013), and topographic data are based on ETOPO1 (Amante & Eakins 2009). SvS acknowledges support from the DFG research training group 'Natural Hazards and Risks in a Changing World' (Grant No. GRK 2043/1). We also like to thank Anne Strader and an anonymous reviewer for improving the manuscript.

REFERENCES

Amante, C. & Eakins, B.W., 2009. *ETOPO1 1 arc-minute global relief model: procedures, data sources and analysis*.

Angelier, J., 1979. Determination of the mean principal directions of stresses for a given fault population, *Tectonophysics,* **56**(3–4), T17–T26.

Angelier, J., 2002. Inversion of earthquake focal mechanisms to obtain the seismotectonic stress IV-a new method free of choice among nodal planes, *Geophys. J. Int.,* **150**(3), 588–609.

Armijo, R., Carey, E. & Cisternas, A., 1982. The inverse problem in microtectonics and the separation of tectonic phases, *Tectonophysics,* **82**(1-2), 145–160.

Bird, P., 2003. An updated digital model of plate boundaries, *Geochem. Geophys. Geosyst.,* **4**(3), 1991.

Bott, M.H.P., 1959. The mechanics of oblique slip faulting, *Geol. Mag.,* **96**(02), 109.

Byerlee, J., 1978. Friction of rocks, *Pure appl. Geophys.,* **116**(4-5), 615–626.

Cardinali, C., Pezzulli, S. & Andersson, E., 2004. Influence-matrix diagnostic of a data assimilation system, *Q. J. R. Meteorol. Soc.,* **130**(603), 2767–2786.

Carey-Gailhardis, E. & Brunier, B., 1974. Analyse théorique numerique d'un modèle mécanique élementaire appliqué à l'étude d'une population des failles, *C. R. Acad. Sci.,* **279,** 891–894.

Cook, R.D., 1977. Detection of influential observation in linear regression, *Technometrics,* **19**(1), 15, doi:10.2307/1268249.

Dempster, A.A., Laird, N.N. & Rubin, D.D.B., 1977. Maximum likelihood from incomplete data via the EM algorithm, *J. R. Stat. Soc. B,* **39**(1), 1–38.

Dziewonski, A.M., Chou, T.-A. & Woodhouse, J.H., 1981. Determination of earthquake source parameters from waveform data for studies of global and regional seismicity, *J. geophys. Res.,* **86,** 2825–2852.

Ekström, G., Nettles, M. & Dziewoński, A.M., 2012. The global CMT project 2004-2010: centroid-moment tensors for 13 017 earthquakes, *Phys. Earth planet. Inter.,* **200-201,** 1–9.

García, D., Wald, D.J. & Hearne, M.G., 2012. A global earthquake discrimination scheme to optimize ground-motion prediction equation selection, *Bull. seism. Soc. Am.,* **102**(1), 185–203.

Gephart, J.W. & Forsyth, D.W., 1984. An improved method for determining the regional stress tensor using earthquake focal mechanism data: application to the San Fernando Earthquake Sequence, *J. geophys. Res.,* **89**(B11), 9305.

Hardebeck, J.L. & Hauksson, E., 1999. Role of fluids in faulting inferred from stress field signatures, *Science,* **285**(5425), 236–239.

Hardebeck, J.L. & Hauksson, E., 2001a. Stress orientations obtained from earthquake focal mechanisms: what are appropriate uncertainty estimates? *Bull. seism. Soc. Am.,* **91**(2), 250–262.

Hardebeck, J.L. & Hauksson, E., 2001b. Crustal stress field in southern California and its implications for fault mechanics, *J. geophys. Res.,* **106**(B10), 21 859–21 882.

Hardebeck, J.L. & Michael, A.J., 2004. Stress orientations at intermediate angles to the San Andreas Fault, California, *J. geophys. Res.,* **109,** B11.

Hardebeck, J.L. & Michael, A.J., 2006. Damped regional-scale stress inversions: methodology and examples for southern California and the Coalinga aftershock sequence, *J. geophys. Res.,* **111**(B11), doi:10.1029/2005JB004144.

Hill, R.W. & Holland, P.W., 1977. Two robust alternatives to least-squares regression, *J. Am. Stat. Assoc.,* **72**(360), 828–833.

Hoaglin, D.C. & Welsch, R.E., 1978. The hat matrix in regression and ANOVA, *Am. Stat.,* **32**(1), 17, doi:10.1080/00031305.1978.10479237.

Holland, P.W. & Welsch, R.E., 1977. Robust regression using iteratively reweighted least-squares, *Commun. Stat. - Theory Methods,* **6**(9), 813–827.

Kagan, Y.Y., 1990. Random stress and earthquake statistics: spatial dependence, *Geophys. J. Int.,* **102**(3), 573–583.

Kagan, Y.Y., 1991. 3-D rotation of double-couple earthquake sources, *Geophys. J. Int.,* **106**(3), 709–716.

Kagan, Y.Y., 1992. Correlations of earthquake focal mechanisms, *Geophys. J. Int.,* **110**(2), 305–320.

Kagan, Y.Y., 2000. Temporal correlations of earthquake focal mechanisms, *Geophys. J. Int.,* **143**(3), 881–897.

Kagan, Y.Y., 2007. Simplified algorithms for calculating double-couple rotation, *Geophys. J. Int.,* **171**(1), 411–418.

Kagan, Y.Y., 2013. Double-couple earthquake source: symmetry and rotation, *Geophys. J. Int.,* **194**(2), 1167–1179.

Kagan, Y.Y. & Knopoff, L., 1985. The two-point correlation function of the seismic moment tensor, *Geophys. J. Int.,* **83**(3), 637–656.

Lisle, R.J., 2013. A critical look at the Wallace–Bott hypothesis in fault-slip analysis, *Bull. Soc. Geol. France,* **184**(4-5), 299–306.

Lund, B. & Slunga, R., 1999. Stress tensor inversion using detailed microearthquake information and stability constraints: application to Ölfus in southwest Iceland, *J. geophys. Res.,* **104**(B7), 14 947–14 964.

Martínez-Garzón, P., Ben-Zion, Y., Abolfathian, N., Kwiatek, G. & Bohnhoff, M., 2016. A refined methodology for stress inversions of earthquake focal mechanisms, *J. geophys. Res.,* **121**(12), 8666–8687.

Maury, J., Cornet, F.H. & Dorbath, L., 2013. A review of methods for determining stress fields from earthquakes focal mechanisms; application to the Sierentz 1980 seismic crisis (Upper Rhine graben), *Bull. Soc. Geol. France,* **184**(4-5), 319–334.

McKenzie, D.P., 1969. The relation between fault plane solutions for earthquakes and the directions of the principal stresses, *Bull. seism. Soc. Am.,* **59**(2), 591–601.

Menke, W., 2012. *Geophysical Data Analysis: Discrete Inverse Theory,* MATLAB, edn, Academic Press, Vol. **45**.

Michael, A.J., 1984. Determination of stress from slip data: faults and folds, *J. geophys. Res.,* **89**(B13), 11 517–11 526.

Michael, A.J., 1987. Use of focal mechanisms to determine stress: a control study, *J. geophys. Res.,* **92**(B1), 357,

Michael, A.J., 1991. Spatial variations in stress within the 1987 Whittier Narrows, California, aftershock sequence: new techniques and results, *J. geophys. Res.,* **96**(B4), 6303.

Pardo, M., Comte, D. & Monfret, T., 2002. Seismotectonic and stress distribution in the central Chile subduction zone, *J. South Am. Earth Sci.,* **15**(1), 11–22.

Rivera, L. & Cisternas, A., 1990. Stress tensor and fault plane solutions for a population of earthquakes, *Bull. seism. Soc. Am.,* **80**(3), 600–614.

Sanderson, C. & Curtin, R., 2016. Armadillo: a template-based C++ library for linear algebra, *J. Open Source Softw.,* **1,** 26, .

Specht, S., Heidbach, O., Cotton, F. & Zang, A., 2017, Data-driven earthquake focal mechanism cluster analysis, Tech. rep., GFZ German Research Centre for Geosciences, Potsdam.

Street, J.O., Carroll, R.J. & Ruppert, D., 1988. A note on computing Robust regression estimates via iteratively reweighted least squares, *Am. Stat.,* **42**(2), 152, doi:10.7289/V5C8276M.

Tarantola, A., 2005. *Inverse Problem Theory and Methods for Model Parameter Estimation,* SIAM.

Townend, J. & Zoback, M.D., 2001. Implications of earthquake focal mechanisms for the frictional strength of the San Andreas fault system, *Geol. Soc., London, Spec. Publ.,* **186,** 13–21.

Vavryčuk, V., 2011. Principal earthquakes: theory and observations from the 2008 West Bohemia swarm, *Earth planet. Sci. Lett.,* **305**(3–4), 290–296.

Wallace, R.E., 1951. Geometry of shearing stress and relation to faulting, *J. Geol.,* **59**(2), 118–130.

Wessel, P., Smith, W. H.F., Scharroo, R., Luis, J. & Wobbe, F., 2013. Generic mapping tools: improved version released, *EOS, Trans. Am. geophys. Un.,* **94**(45), 409–410.

Xu, P., 2004. Determination of regional stress tensors from fault-slip data, *Geophys. J. Int.,* **157**(3), 1316–1330.

Zaliapin, I. & Ben-Zion, Y., 2011. Asymmetric distribution of aftershocks on large faults in California, *Geophys. J. Int.,* **185**(3), 1288–1304.

Zaliapin, I., Gabrielov, A., Keilis-Borok, V. & Wong, H., 2008. Clustering analysis of seismicity and aftershock identification, *Phys. Rev. Lett.,* **101**(1), 4–7.

Zang, A. & Stephansson, O., 2010. *Stress Field of the Earth's Crust,* Springer Science & Business Media.